Localized metabolomic gradients in patient-derived xenograft models of glioblastoma

Published in final edited form as:

Cancer Res. 2020 March 15; 80(6): 1258–1267. doi:10.1158/0008-5472.CAN-19-0638.

Localized metabolomic gradients in patient-derived xenograft models of glioblastoma

Elizabeth C. Randall[1], **Begoña G. C. Lopez**[2], **Sen Peng**[3], **Michael S. Regan**[2], **Walid M. Abdelmoula**[2], **Sankha S. Basu**[4], **Sandro Santagata**[4], **Haejin Yoon**[5], **Marcia C. Haigis**[5], **Jeffrey N. Agar**[6], **Nhan L. Tran**[7], **William F. Elmquist**[8], **Forest M. White**[9], **Jann N. Sarkaria**[10], **Nathalie Y. R. Agar**[1,2,11]

[1]Department of Radiology, Brigham and Women's Hospital, Harvard Medical School, Boston, MA 0211

[2]Department of Neurosurgery, Brigham and Women's Hospital, Harvard Medical School, Boston, MA 02115

[3]Cancer and Cell Biology Division, Translational Genomics Research Institute – Affiliate of City of Hope, Phoenix, AZ 85004

[4]Department of Pathology, Brigham and Women's Hospital, Harvard Medical School, Boston, MA 02115

[5]Department of Cell Biology, Harvard Medical School, Boston, 02115

[6]Department of Chemistry and Chemical Biology, Northeastern University, 412 TF (140 The Fenway), Boston, MA 02111

[7]Department of Cancer Biology, Mayo Clinic, 13400 E. Shea Blvd. MCCRB 03-055, Scottsdale, Arizona 85259

[8]Department of Pharmaceutics, College of Pharmacy, University of Minnesota, Minneapolis, MN 55455

[9]Department of Biological Engineering, Koch Institute for Integrative Cancer Research, Massachusetts Institute of Technology, 500 Main St, Cambridge, MA 02142

[10]Department of Radiation Oncology, Mayo Clinic, 200 First St SW, Rochester MN 55902

[11]Department of Cancer Biology, Dana-Farber Cancer Institute, Harvard Medical School, Boston, MA 02115

Abstract

Glioblastoma (GBM) is increasingly recognized as a disease involving dysfunctional cellular metabolism. GBMs are known to be complex heterogeneous systems containing multiple distinct cell populations and are supported by an aberrant network of blood vessels. A better understanding of glioblastoma metabolism, its variation with respect to the tumor microenvironment, and

Corresponding Author: Nathalie Y. R. Agar, Department of Neurosurgery, Brigham and Women's Hospital, Harvard Medical School, Boston, MA 02115, 617-525-7374, Nathalie_Agar@dfci.harvard.edu.

Conflict of Interest: N.Y.R.A. is a scientific advisor to BayesianDx and inviCRO.

resulting regional changes in chemical composition is required. This may shed light on the observed heterogeneous drug distribution which cannot be fully described by limited or uneven disruption of the blood brain barrier. In this work we used mass spectrometry imaging (MSI) to map metabolites and lipids in patient-derived xenograft models of glioblastoma. A data analysis workflow revealed that distinctive spectral signatures were detected from different regions of the intracranial tumor model. A series of long-chain acylcarnitines were identified and detected with increased intensity at the tumor edge. A 3D MSI dataset demonstrated that these molecules were observed throughout the entire tumor/normal interface and were not confined to a single plane. mRNA sequencing demonstrated that hallmark genes related to fatty acid metabolism were more highly expressed in samples with higher acyl-carnitine content. These data suggest that cells in the core and the edge of the tumor undergo different fatty acid metabolism, resulting in different chemical environments within the tumor. This may influence drug distribution through changes in tissue drug affinity or transport, and constitute an important consideration for therapeutic strategies in the treatment of GBM.

Keywords

glioblastoma; tumor metabolism; metabolomics; microenvironment; pharmacokinetics

Introduction

Glioblastoma (GBM) is a highly malignant and invasive form of brain tumor (1). Typical treatment for GBM only minimally delays the course of the disease and as such there is a substantial need for new therapies and therapeutic targets. The lack of progress in developing therapeutics for GBM is due to a combination of factors including limited and heterogeneous drug delivery across both the blood-brain and the aberrant blood-tumor barriers (BBB and BTB) (2-4). In a previous study by this group, the relationship between drug distribution and drug response in GBM patient derived xenografts (PDX) models was examined in relation to the breakdown of the BBB and contrast enhancement by MRI (5). A mutation which occurs in 50% of GBMs is amplification of the epidermal growth factor receptor (EGFR) (6). The EGFR tyrosine kinase inhibitor erlotinib, which has been tested as a potential treatment for GBM, was mapped in PDX models and was correlated with multimodality data including phospho-proteomics and mRNA sequencing. This demonstrated that, due to a combination of limitations imposed by the BBB and tissue characteristics, the concentration of erlotinib measured in the intracranial tumor, was insufficient to successfully inhibit EGFR tyrosine kinase signaling. During this study an interesting distribution of global lipid signal was highlighted by stimulated Raman scattering microscopy, with higher drug concentrations detected in regions of lower lipid content (5). Regional variation in lipid content caused by differences in metabolism and cellular content could play a role in drug distribution, and hence this relationship, along with an observed decrease in erlotinib concentration measured at the tumor edge is the subject of the study described herein.

Tumor cells are surrounded by the tumor microenvironment; defined as the non-tumor cells, molecules and blood vessels that surround and feed a tumor cell (7). To fulfill the demands

of biomass formation, proliferating cells increase their uptake of nutrients and reprogram glycolysis (8). The metabolism of each tumor cell is therefore dependent on the availability of nutrients in the microenvironment. The molecular composition of the microenvironment for each tumor cell varies depending on its location in the tumor mass and proximity to blood vessels (9). Cancer cells are programmed to increase the uptake of glucose, but a smaller proportion of this is oxidized in the Krebs cycle to produce ATP; instead cancer cells use glucose for anabolic processes (10). Fatty acids are an additional energy source, and can be metabolized to produce ATP – providing twice as much energy as carbohydrates (10). Recent reports have suggested that ATP production via fatty acid oxidation is required for the respiration and proliferation of malignant glioma cells (11), however, much about how different cells within tumor volumes utilize different metabolic pathways remains unknown. Whilst the GBM microenvironment shares some commonalities with other solid tumors, such as immune cells, blood vessels and the extracellular matrix, the tumor microenvironments of brain tumors also contain microglia and astrocytes and a substantially different metabolic milieu compared with tumors in other organs (7). In addition, a number of metabolic phenotypes exist amongst GBM; it is therefore necessary to understand intra- and inter-tumor metabolic heterogeneity.

To understand the association between tumor metabolism and drug efficacy, the spatial relationships between drugs and biomolecules is needed, both within the tumor as well as in the surrounding microenvironment. Matrix assisted laser desorption/ionization (MALDI) mass spectrometry imaging (MSI) is a label-free technique capable of spatial detection and mapping of hundreds to thousands of molecules (12). MALDI MSI has been used in numerous metabolomic and lipidomic studies of cancerous tissues (13-15), and has also been used for the simultaneous analysis of drugs and drug metabolites with endogenous biomolecules, and potential markers of therapeutic response (16, 17). High mass resolution MALDI MSI of proteins and metabolites in a mouse model of GBM was reported by Dilillo *et al.*(18), where they were able to map numerous proteins and metabolites via different sample preparation techniques, and found metabolic differences between healthy and tumor brain tissues (18).

In this report we used MALDI Fourier transform ion cyclotron resonance (FT ICR) MSI to image lipids and metabolites in four different PDX models of GBM. Differences between normal brain and tumor tissue were apparent, as well as distinctive sub-regions within the tumor. A series of long chain acylcarnitines was detected with higher intensity in regions corresponding to the tumor edge. We subsequently investigated the distribution of two drugs, erlotinib and AZD1775, in the same PDX models, and mapped them relative to markers of metabolism and tumor vasculature.

Materials and Methods

Animals and Tissue sample preparation

All studies involving animals were reviewed and approved by the Institutional Animal Care and Use Committee at Mayo Clinic. For full details of patient-derived xenograft model preparation see Supplementary Information. Briefly, xenografts were established in female athymic nude mice. A subset of mice were dosed with a single dose of erlotinib (100 mg/kg)

or AZD1775 (200 mg/kg). Mice were euthanized (dosed animals 2 hours post-dose) and brains were harvested and flash frozen on dry ice. Tissues were stored at −80°C prior to analysis. Tissues were placed at −25°C 1 h before use, and tissue sections were prepared using a Microm HM550 cryostat (Thermo Scientific™, Waltham, MA) with the microtome chamber chilled at −21°C and the specimen holder at −19°C. Tissue sections of 12 μm thickness were thaw mounted onto ITO-coated microscopic slides (Bruker Daltonics, Billerica, MA) for MALDI MSI and onto glass slides for either liquid extraction surface analysis (LESA) MS/MS or hematoxylin and eosin (H&E) staining. H&E microscopy images were acquired using a Zeiss Observer Z.1 microscope equipped with 20x Plan-APOCHROMAT lens and AxioCam MR3 camera. The mounted tissue sections were dried for 15 minutes in a desiccator prior to matrix application. 2,5-dihydroxybenzoic acid matrix (160 mg/mL solution in methanol/0.1% TFA/DMSO 69.3:29.7:1 vol/vol/vol) was deposited using a TM-sprayer (HTX imaging, Carrboro, NC) with the following conditions: flow rate, 0.09 mL/min, spray nozzle velocity, 1200 mm/min, spray nozzle temperature, 75°C, nitrogen gas pressure of 10 psi, track spacing of 2 mm and 4 passes. In order to investigate regional ion suppression, deuterium labelled palmitoylcarnitine was coated over a series of tissue sections from intracranial GBM12 PDX models. A solution of Palmitoyl-L-carnitine-(n-methyl-D_3) (20 μM in 50/50 methanol/water v/v), (Sigma-Aldrich, St. Louis, MO) was deposited using the TM-Sprayer with a flow rate of 0.09 mL/min, spray nozzle velocity of 1200 mm/min, spray nozzle temperature of 75°C, nitrogen gas pressure of 10 psi, track spacing 2 mm and 2 passes. A solution of erlotinib-(D_6) (1 μg/mL, in methanol), was coated over a further set of tissue specimens under the same TM-Sprayer conditions. The concentration of internal standard and spray parameters were optimized so that it could be detected without saturating the signal.

MALDI FT-ICR mass spectrometry imaging

Mass spectrometry imaging data were acquired using a 9.4 Tesla SolariX XR FT-ICR MS (Bruker Daltonics, Billerica, MA) externally calibrated in electrospray ionization positive ion mode using a tuning mix solution (Agilent Technologies, Santa Clara, CA). MALDI MS images were acquired with a pixel step size of 100 μm. Spectra were acquired in positive ion mode with 250 laser shots accumulated at each location. Spectra were collected in the range *m/z* 100-3000 with isolation of ions using the constant accumulation of selected ions (CASI) mode, with Q1 set to 500 and an isolation window of 260. Online calibration of spectra to heme (*m/z* 616.17668, Δppm tolerance 200, intensity threshold 500) was applied. The laser focus was set to ‘small’, the laser energy was set to 35% (arbitrary scale) with a laser frequency of 1000 Hz. MALDI MS images were acquired and viewed using FlexImaging 5.0 (Bruker Daltonics, Bremen, Germany).

Data processing and statistical analysis

MSI data were analyzed using SCiLS Lab software (Buker Daltonics, Bremen, Germany). Data were normalized to total ion intensity (TIC) and were reduced to a peak list of ~500 *m/z* most relevant values. This peak list was created by correlating each spectrum with different peaks at different positions in the image, based on the orthogonal matching pursuit (OMP), and automatically finding the most correlated peaks. Bisecting *k*-means clustering (using the correlation distance metric) was used to provide segmented images showing

regions of spectral similarity. Regions of interest (corresponding to tumor core and tumor edge) were defined based on the resulting segmentation map and receiver operating characteristic (ROC) analysis was performed to find ions which discriminated between tumor core and tumor edge. *m/z* values with an area under the curve (AUC) > 0.75 were searched against publicly available databases (LIPID MAPS and the Human Metabolome Database (HMDB)) (19, 20). Ions were preliminarily identified if assignments were associated with Δppm <2. Further characterization of ions preliminarily identified as acylcarnitines was performed by MS/MS.

Liquid extraction surface analysis (LESA) MS/MS

Serial sections to those analyzed by MALDI MSI were used for LESA MS/MS structural confirmation. Adjacent to the tissue on the glass slide were placed 0.5 μL dried droplets of standards of: Myristoyl-L-carnitine, Palmitoyl-L-carnitine and Stearoyl-L-carnitine (10 μM, in water), (Sigma-Aldrich Inc., Milwaukee, WI). LESA was performed using the TriVersa NanoMate (Advion) system coupled via nano-electrospray ionization (nano-ESI) to an amaZon Speed ion trap mass spectrometer (Bruker Daltonics, Billerica, MA). Sampling locations were selected within the tumor edge region (as determined from H&E staining of a serial section) or from dried droplets of each standard. The extraction/ESI solvent system was (60/40 methanol/0.1% formic acid v/v). Solvent (3 μL) was aspirated from a reservoir into a conductive pipette tip. The tip relocated to a pre-defined position 1 mm above the sample and dispensed 0.7 μL solvent onto the surface. The liquid microjunction was maintained for 5 seconds to allow soluble analytes to dissolve before 1 μL was re-aspirated; this extraction process was repeated once and then injected into the mass spectrometer via nano-ESI, with a gas pressure of 0.3 psi and a tip voltage of 1.4 kV. Mass spectra were acquired for 5 minutes, in the positive ion mode, with an *m/z* range of 100 – 1100 and the ion trap target tuned to *m/z* 400. After an initial 30 second acquisition of full scan MS, MS/MS was performed for the protonated species of each acylcarnitine as follows: myristoylcarnitine parent mass was *m/z* 372.3, palmitoylcarnitine parent mass was *m/z* 400.3 and stearoylcarnitine parent mass was *m/z* 428.3, all three species were fragmented with an isolation window of 2.0 and reaction amplitude 1.7.

RNA Sequencing and analysis

ArcturusXT™ LCM System was used to capture cells from intracranial tumor section. Total RNA was isolated using RNAeasy Mini Kit (Qiagen), and then processed through the RNA Clean & Concentrator-5 kit (Zymo Research) according to manufacturer's protocols. Total RNA (50 ng) was used to generate whole transcriptome libraries for RNA sequencing using Illumina's TruSeq RNA Sample Prep. Poly(A) mRNA selection was performed using oligo(dT) magnetic beads, and libraries were enriched using the TruSeq PCR Master Mix and primer cocktail. Amplified products were cleaned and quantified using the Agilent Bioanalyzer and Invitrogen Qubit. The clustered flowcell was sequenced on the Illumina HiSeq 4000 for paired 100-bp reads using Illumina's TruSeq SBS Kit V3. Lane level fastq files were appended together if they were sequenced across multiple lanes. The mouse reads were filtered out using in-silico method after sequencing. We used xenome (21) tool to classify reads into human, mouse, both, unmapped, and ambiguous categories. Human-only category reads were kept for downstream analysis. These processed fastq files were then

aligned with STAR aligner using reference gene annotation (GTF) file. Transcript abundance was quantified and normalized using Salmon in the unit of transcripts per million (TPM). Consensus clustering was performed using ConsensusClusterPlus R package and heatmaps were generated using R heatmap.2 package with Euclidean Distance and average clustering method. Gene set variation analysis (GSVA)(22) was then performed to determine the change and variation in pathway activities of glycolysis and fatty acid metabolism gene sets. Those genesets were downloaded from Molecular Signatures Database (MSigDB) (23). Log transformation was applied and default parameter settings were followed for RNAseq data in GSVA. mRNA sequencing data has been deposited in EMBL-EBI European Nucleotide Archive (ENA) database (accession number PRJEB35120).

Results

Metabolic differences between tumor core and tumor edge in intracranial GBM12 PDX models

Metabolomic MALDI MSI was performed on brain tissue sections from three different GBM12 PDX animals (Figure 1). A segmentation map produced via bisecting *k*-means clustering (as described in methods section) detected differences in mass spectra between gray and white matter in the brain, between tumor and healthy brain tissue and between two different regions of the GBM tumor (see Figure 1a & 1b). The tumor region was delineated by standard histopathology on a serial section of tissue. The segmentation map produced with $k = 8$ indicates two metabolically different regions of the tumor, one in the core of the tumor and one at the outer edge, labelled in white and blue, respectively. Receiver operating characteristic (ROC) analysis was applied to the reduced peak list in order to elucidate which ions in the mass spectra contribute to this difference. Ions with an ROC area under the curve (AUC) >0.75 were searched against LIPID MAPS and HMDB and candidate identities were proposed (for annotated peaklists see Supplementary datafile 1). A number of ions highlighted via this analysis were identified as long chain acylcarnitines. The Δppm associated with these assignments were all <2, which can be expected from high mass resolution FT ICR MS data. Hypothesis testing by a t-test indicated that the difference in average intensity of each acylcarnitine was associated with a p-value in most cases <0.001 and in all cases <0.05 (see Table 1). A total of seven different acylcarnitines were identified through this analysis, all demonstrating a similar spatial distribution within the tumor. MALDI ion images of three of the most abundant long chain acylcarnitines: myristoylcarnitine, palmitoylcarnitine and stearoylcarnitine, are displayed in Figure 1c - 1e. All three species were detected with higher intensity in the tumor edge compared with the tumor core. Structural confirmation of these ions was performed by LESA MS/MS (see Supplementary results *and* Supplementary Figure S1). Incorporation of the internal standard palmitoylcarnitine-(N-methyl-d3), according to the method proposed by Taylor *et al.*(24), into the matrix provided evidence to suggest that increased intensity of acylcarnitine was not observed due to differential ion suppression (see Supplementary results *and* Supplementary Figure S2a-d).

3D MALDI MSI demonstrates that acylcarnitines are detected with increased intensity at the entire infiltrative tumor edge

Sequential coronal tissue sections were taken in increments of 160 μm throughout the tumor containing portion of an independent GBM12 PDX animal. These 22 sections were imaged using MALDI MSI to investigate the distribution of acylcarnitines throughout the entire tumor volume. All acylcarnitine species identified in this work were found to have the same distribution within tissue (see Supplementary Figure S3), therefore example images of palmitoylcarnitine are presented here as a proxy for all long chain acylcarnitines. Acylcarnitines were detected with increased intensity at the edge of the tumor and at the interface between tumor and normal tissue, see Figures 2a & 2b. These data demonstrate that this phenomenon was not peculiar to a single anomalous plane within the tumor of one animal. 3D reconstructions of MALDI ion images show the distribution of acylcarnitine within the tumor volume and demonstrate the location of the tumor relative to the vasculature and blood – via overlay with ion images of heme (25), Figure 2c - 2e. A further set of images was acquired from six animals of the same GBM12 PDX model, tissue sections were acquired from roughly the same depth within the tumor, Supplementary Figure S4. Similar distributions of acylcarnitines were measured in all six animals. Acylcarnitines were only detected with higher intensity at the interface between tumor and normal tissue, and not detected in portions of the tumor adjacent to the outer edge of the brain.

Distinctive and different distribution and relative abundance of acylcarnitines is observed in four different GBM PDX models

In order to establish whether this phenomenon was observed in other models of GBM, tissues from four different GBM PDX models, GBM12, GBM22, GBM39 and GBM108 (n=2), were prepared and analyzed by MALDI MSI, see Figure 3. Tumor regions were delineated using a combination of H&E and MALDI MSI data segmentation; see Figure 3a & b. Acylcarnitines were detected in all four models, with the highest relative intensity detected in GBM12, followed by GBM22, GBM39 and GBM108 in order of decreasing intensity, as shown in Figure 3c. In all eight animals of the four models, acylcarnitines were detected with higher intensity at the tumor edge. In some cases, localized spots of higher intensity were detected in central regions of the tumors, for example in GBM22.

Acylcarnitine and ATP demonstrate inverse distributions in four different GBM PDX models

The distribution of other ions which might act as functional markers was investigated in relation to acylcarnitine. Heme, a cofactor of hemoglobin, adenosine triphosphate (ATP) and palmitoylcarnitine were visualized alongside H&E images of serial sections of the four GBM models studied, see Figure 4. Ion images of heme allow visualization of the brain vasculature and blood - indicating the location, size and density of blood vessels relative to anatomical features of the brain and the tumor (see Supplementary Figure S5). The highest relative intensity of heme was detected from GBM108 PDX models, which was expected due to the highly vascular nature of GBM108. Higher intensity of heme was detected from the VEGF+ GBM108 PDX, see Figure 4. ATP (assignment associated with Δppm = 0.01) was detected with higher intensity in tumor tissue compared with normal tissue, in all

models. In normal brain tissue, higher intensity of ATP was detected in the hippocampus and white matter tracts, consistent with previous findings and supporting the identity of these ions (26). A side-by-side comparison of images of ATP and palmitoylcarnitine suggest an inverse relationship within the tumor, whereby high intensity of acylcarnitine is detected in regions of low intensity ATP and vice versa. Regions of higher acylcarnitine intensity in the tumor cores (for example in GBM22 and GBM108 VGEF-seem to correspond with regions of higher heme intensity), raising the possibility that the vasculature plays a role in the distribution of acylcarnitine. In cases of hypervascularization as in VGEF+, the distribution of heme and acylcarnitine were visually more different.

Fatty acid metabolism upregulated in GBM PDX models with high acylcarnitine content and inverse relation with glycolysis

To further probe the metabolic processes taking place in the tumors, and relate them to the content of acylcarnitines and ATP levels, analysis by mRNA sequencing was performed. Based on the heatmaps highlighting the activated genes within pathways for fatty acid metabolism and glycolysis (Supplementary datafiles 2 & 3), a score was calculated for each GBM PDX model, and is represented in the gene set variation analysis (GSVA) plot, see Figure 5. The levels of palmitoylcarnitine and ATP (measured by MALDI FT ICR MSI), Figure 5a & 5b, are displayed alongside GSVA plots for fatty acid metabolism and glycolysis respectively, Figure 5c & 5d, for each specimen. In this blinded experiment, transcriptome data from the mice was eliminated to analyze only the human (tumor) gene expression. Then validation of samples' relationship was performed using consensus clustering, and heatmaps were used to visualize the similarity between the samples with respect to fatty acid metabolism and glycolysis, using MSigDB gene sets for those pathways. A list of upregulated genes was selected to obtain the GSVA score. Hallmark genes related to fatty acid metabolism were found to have higher expression in the samples with higher measured levels of acylcarnitine (GBM12), see Figure 5a & c. This relationship was further probed by investigating transcript expression of specific components of the carnitine cycle (CPT1a, CPT2, CRAT and SLC25A20). Normalized gene expression was plotted for CPT1a, CPT2, CRAT and SLC25A20, for each GBM PDX model, see Supplementary Figure S6a & b. It was found that the expression levels of these genes were broadly in agreement with measured levels of acylcarnitine, with GBM12 demonstrating the highest expression of CPT1a and SLC25A20. CPT2 demonstrated little difference in expression between the different GBM models. GBM108 demonstrated the lowest expression of CPT1a, CRAT and SLC25A20. Hallmark genes associated with glycolysis were most highly expressed in GBM108 VGEF -, and one of the samples of GBM39. This was in agreement with higher levels of ATP in these specimens, as measured by MALDI FT-ICR MSI, see Figure 5b&d.

Drug distribution relative to structural and functional markers was visualized by MALDI MSI

The distribution of two different drugs, erlotinib and AZD1775, was investigated in three different PDX models of GBM, Figure 6, MS images of both drugs are displayed alongside structural and functional markers: palmitoylcarnitine, ATP and heme. Both drugs were detected with higher intensity in tumor regions of all the GBM models. Erlotinib, an

epidermal growth factor receptor (EGFR) inhibitor, was detected with lower intensity at the tumor edge, characterized by a dark ring around the tumor, in GBM12 models. Palmitoylcarnitine was detected with higher intensity in this region, demonstrating a somewhat inverse distribution, see overlay images in Supplementary figure S7. AZD1775, a WEE1 kinase inhibitor (with a key role on the Cdk1 protein that regulates the cell cycle at different checkpoints), was detected with a relatively homogeneous distribution throughout the tumor region, with drug detected at the tumor edge with approximately the same intensity as the tumor core. Incorporation of an internal standard (D6-erlotinib) indicated that there was no significant difference in desorption/ionization efficiency between the tumor edge and the tumor core, see Supplementary figure S8a-e. This indicates that the absence of erlotinib in the edges of the tumor was not due to ion suppression in that area. The molecular structures and physicochemical properties of erlotinib and AZD1775 are summarized in Supplementary figure S9. The pH dependent solubility of erlotinib is established (27), where more acidic pH results in maximum efficacy, due to increased solubility of erlotinib (28). Therefore, the pH variation found in glioblastoma might affect the solubility of erlotinib, leading to a heterogeneous distribution of the drug in the tumor. The distribution of heme varied between the three different animals/PDX models. Erlotinib and AZD1775 were found to distribute differently within GBM PDX tumors, which may be linked to their different pH sensitivities.

Discussion

The study described herein investigated spatially resolved metabolism in GBM PDX models. We describe the novel finding of increased intensity of long chain acylcarnitines at the tumor edge, relative to the tumor core. We observed the same distribution amongst seven different long chain acylcarnitines, in eight different animals of the same GBM PDX model and similar distributions in a further two animals of four different GBM models. Differences in the relative abundance of acylcarnitines between the different GBM models was observed and raises the possibility that the tumor type or grade may contribute to these differences, though more extensive studies will be required. Metabolism was mapped in 2D sections and reconstructed in 3D images, demonstrating that the increase in intensity of acylcarnitines was detected at the entire interface between tumor and normal tissue, and was not detected at tumor edges which extended to the edge of the brain. This suggests that the increase in acylcarnitine content delineates an interface between normal and tumor cells. Utilizing stable isotope internal standards, we suggest that the increase in acylcarnitine intensity at the tumor edge was not explained by ion suppression or technical artifact.

Long chain acylcarnitines are activated molecules involved in the transport of long chain fatty acids across mitochondrial membranes after which they can undergo β-oxidation to produce ATP. Glucose has been traditionally considered the primary energy source for the adult brain under normal conditions, however, there is evidence to suggest that fatty acids are also used by normal brain tissue (29). This is perhaps supported by our detection of acylcarnitines in the white matter tracts of the normal mouse brain. It has previously been demonstrated that human GBM tumors require fatty acid oxidation for respiration and proliferation and inhibition of FAO prolonged survival in a syngeneic mouse model of malignant glioma (11). Rewiring of metabolic programs, such as aerobic glycolysis and

increased glutamine metabolism, are crucial for cancer cells to shed from a primary tumor, overcome the nutrient and energy deficit, and eventually survive and form metastases. However, the role of lipid metabolism in the aggressive phenotype of malignant cancers remains unclear. Our observation of different abundance of acylcarnitine at the tumor edge vs the core suggests that different regions of the tumor are undergoing different relative levels of FAO. Furthermore, analysis by RNA sequencing suggests that GBM PDX models with higher acylcarnitine content also demonstrate upregulated fatty acid metabolism.

Significant research on the properties and functions of acylcarnitines has focused on metabolism, i.e. shuttling fatty acids for β-oxidation; however, there is a body of work demonstrating that acylcarnitines play roles in neuroprotection and signaling. Most of these studies have focused on L-carnitine (LC) and acetyl-L-carnitine (ALC) and not the esterified derivatives, however, the carnitine portion, which is common to all three species, has antioxidant and anti-apoptotic functions. The roles of palmitoyl-L-carnitine (PLC) in the brain have also been studied, with PLC thought to influence membrane fluidity due to its amphiphilic nature and ability to react on membrane surfaces. PLC has also been found to stimulate the expression of GAP-43, a protein which is involved in neuroplasticity and neurotransmission (30). It is possible that the accumulation of acylcarnitines at the tumor edge provides protection to tumor cells in this region, resulting in an overall survival benefit to the tumor. The pro-inflammatory properties of long chain acylcarnitines (31) were recently discussed in a report detailing the accumulation of long chain acylcarnitines at the periphery of a spinal cord injury site in rat. The striking distribution of acylcarnitines was correlated with the presence of microglia in tissue surrounding the injury site (32). It is possible that a similar inflammatory response is triggered by the presence of acylcarnitines in the GBM PDX tumor. The multiple roles played by acylcarnitines should be considered in future studies to elucidate the mechanism of action of acylcarnitine in GBM – beyond β-oxidation.

Finally, we investigated the distribution of two different drug compounds both of which have been investigated in the possible therapeutic treatment of GBM, with different mechanisms of action and physicochemical properties, in three different GBM models. Erlotinib, whose solubility is known to be pH sensitive (27), was detected with higher intensity in the tumor core, and lower intensity at the tumor margin. Lower intensity of acylcarnitine was detected in GBM39 (relative to GBM12) and the inverse association between acylcarnitines and erlotinib was to a lesser degree. Conversely, AZD1775 was detected with a relatively homogeneous distribution throughout the tumor. It is well established that tumors generally have a lower pH than their surrounding tissue. A study using MRI based pH measurement found that in rat glioma models, the tumor core was more acidic than the tumor edge (33). The pH of the extracellular space in tumors varies between 6.5 and 7.5 (34). Tumor acidosis is intricately linked with tumor metabolism, with the increased production and accumulation of H^+ via increased lactic acid production and hydration of CO_2 produced via oxidative metabolism (35). Acidic tumor environments have also been shown to promote FAO via the downregulation of acetyl-CoA carboxylase 2 (ACC2) (35). This raises the possibility that the observed distribution of erlotinib is influenced by spatial differences in tumor pH, as a result of variation in metabolism.

In summary we have identified a class of molecules which are highly abundant at the proliferating/infiltrative edge of the tumor in four different PDX models of GBM. Our data demonstrate that the metabolomic composition of the tumor edge is different from that of the tumor core. We suggest that GBM cells at the infiltrative tumor edge undergo different relative levels of FAO, an energy production pathway which has recently been shown to be essential for the respiration and proliferation of glioma cells. The various roles of acylcarnitines beyond FAO should be considered in future work to determine the full implications of this characteristic distribution, and the possible survival advantage that acylcarnitines could provide.

Supplementary Material

Refer to Web version on PubMed Central for supplementary material.

Acknowledgements

This work was funded by NIH U54 CA210180 MIT/Mayo Physical Science Oncology Center for Drug Distribution and Drug Efficacy in Brain Tumors, and by the Dana-Farber Cancer Institute PLGA Fund. NYRA receives support from the Ferenc Jolesz National Center for Image Guided Therapy NIH P41-EB-015898. NYRA also receives support from NIH R01CA201469. ECR is in receipt of an NIH R25 (R25 CA-89017) Fellowship in partnership with the Ferenc Jolesz National Center for Image Guided Therapy at BWH (P41 EB015898). SSB receives support from NIH Training Grant T32 HL007627. The authors thank Dr. Catherine Rawlins, Daniel Donnelly and Nicholas Schmitt for technical assistance with the MALDI FT ICR instrumentation.

References

1. Lin H, et al. (2017) Fatty acid oxidation is required for the respiration and proliferation of malignant glioma cells. Neuro Oncol 19(1):43–54. [PubMed: 27365097]
2. van Tellingen O, et al. (2015) Overcoming the blood–brain tumor barrier for effective glioblastoma treatment. Drug Resist Updat 19:1–12. [PubMed: 25791797]
3. Wang N, Jain RK, Batchelor TT (2017) New Directions in Anti-Angiogenic Therapy for Glioblastoma. Neurotherapeutics:1–12. [PubMed: 27933486]
4. Anjum K, et al. (2017) Current status and future therapeutic perspectives of glioblastoma multiforme (GBM) therapy: A review. Biomed Pharmacother 92:681–689. [PubMed: 28582760]
5. Randall EC, et al. (2018) Integrated mapping of pharmacokinetics and pharmacodynamics in a patient-derived xenograft model of glioblastoma. Nat Commun 9(1):4904. [PubMed: 30464169]
6. Furnari FB, Cloughesy TF, Cavenee WK, Mischel PS (2015) Heterogeneity of epidermal growth factor receptor signalling networks in glioblastoma. Nat Rev Cancer 15(5):302–310. [PubMed: 25855404]
7. Charles NA, Holland EC, Gilbertson R, Glass R, Kettenmann H (2012) The brain tumor microenvironment. Glia 60(3):502–514. [PubMed: 22379614]
8. Palm W, Thompson CB (2017) Nutrient acquisition strategies of mammalian cells. Nature 546(7657):234–242. [PubMed: 28593971]
9. Vaupel P, Kallinowski F, Okunieff P (1989) Blood flow, oxygen and nutrient supply, and metabolic microenvironment of human tumors: a review. Cancer Res 49(23):6449–65. [PubMed: 2684393]
10. Carracedo A, Cantley LC, Pandolfi PP (2013) Cancer metabolism: fatty acid oxidation in the limelight. Nat Rev Cancer 13(4):227–232. [PubMed: 23446547]
11. Lin H, et al. (2017) Fatty acid oxidation is required for the respiration and proliferation of malignant glioma cells. Neuro Oncol 19(1):43–54. [PubMed: 27365097]
12. Cornett DS, Frappier SL, Caprioli RM MALDI-FTICR Imaging Mass Spectrometry of Drugs and Metabolites in Tissue. doi:10.1021/ac800617s.

13. Wang X, et al. (2017) Metabolomic profiling of prostate cancer by matrix assisted laser desorption/ionization-Fourier transform ion cyclotron resonance mass spectrometry imaging using Matrix Coating Assisted by an Electric Field (MCAEF). Biochim Biophys Acta - Proteins Proteomics 1865(7):755–767. [PubMed: 28017863]
14. Shimma S, et al. (2007) MALDI-based imaging mass spectrometry revealed abnormal distribution of phospholipids in colon cancer liver metastasis. J Chromatogr B 855(1):98–103.
15. Clark AR, et al. (2018) Rapid discrimination of pediatric brain tumors by mass spectrometry imaging. J Neurooncol:1–11.
16. Sun N, et al. (2016) Pharmacokinetic and pharmacometabolomic study of pirfenidone in normal mouse tissues using high mass resolution MALDI-FTICR-mass spectrometry imaging. Histochem Cell Biol 145(2):201–211. [PubMed: 26645566]
17. Patterson NH, et al. (2016) Assessment of pathological response to therapy using lipid mass spectrometry imaging. doi:10.1038/srep36814.
18. Dilillo M, et al. (2017) Ultra-High Mass Resolution MALDI Imaging Mass Spectrometry of Proteins and Metabolites in a Mouse Model of Glioblastoma. Sci Rep 7(1):603. [PubMed: 28377615]
19. Wishart DS, et al. (2018) HMDB 4.0: the human metabolome database for 2018. Nucleic Acids Res 46(D1):D608–D617. [PubMed: 29140435]
20. Fahy E, Sud M, Cotter D, Subramaniam S (2007) LIPID MAPS online tools for lipid research. Nucleic Acids Res 35(Web Server issue):W606–12. [PubMed: 17584797]
21. Conway T, et al. (2012) Xenome--a tool for classifying reads from xenograft samples. Bioinformatics 28(12):i172–i178. [PubMed: 22689758]
22. Hänzelmann S, Castelo R, Guinney J (2013) GSVA: gene set variation analysis for microarray and RNA-Seq data. BMC Bioinformatics 14(1):7. [PubMed: 23323831]
23. Liberzon A, et al. (2015) The Molecular Signatures Database Hallmark Gene Set Collection. Cell Syst 1(6):417–425. [PubMed: 26771021]
24. Taylor AJ, Dexter A, Bunch J (2018) Exploring Ion Suppression in Mass Spectrometry Imaging of a Heterogeneous Tissue. Anal Chem 90(9):5637–5645. [PubMed: 29461803]
25. Liu X, et al. (2013) Molecular imaging of drug transit through the blood-brain barrier with MALDI mass spectrometry imaging. Sci Rep 3:2859. [PubMed: 24091529]
26. Kleinridders A, et al. (2018) Regional differences in brain glucose metabolism determined by imaging mass spectrometry. Mol Metab 12:113–121. [PubMed: 29681509]
27. Chu MP, et al. (2015) Gastric Acid Suppression Is Associated With Decreased Erlotinib Efficacy in Non–Small-Cell Lung Cancer. Clin Lung Cancer 16(1):33–39. [PubMed: 25246385]
28. Zhang L, Wu F, Lee SC, Zhao H, Zhang L (2014) pH-Dependent Drug–Drug Interactions for Weak Base Drugs: Potential Implications for New Drug Development. Clin Pharmacol Ther 96(2):266–277. [PubMed: 24733008]
29. Jones LL, McDonald DA, Borum PR (2010) Acylcarnitines: Role in brain. Prog Lipid Res 49(1):61–75. [PubMed: 19720082]
30. Ribas GS, Vargas CR, Wajner M (2014) l-carnitine supplementation as a potential antioxidant therapy for inherited neurometabolic disorders. Gene 533(2):469–476. [PubMed: 24148561]
31. Rutkowsky JM, et al. (2014) Acylcarnitines activate proinflammatory signaling pathways. Am J Physiol Metab 306(12):E1378–E1387.
32. Quanico J, et al. (2018) 3D MALDI mass spectrometry imaging reveals specific localization of long-chain acylcarnitines within a 10-day time window of spinal cord injury. Sci Rep 8(1):16083. [PubMed: 30382158]
33. Maritim S, et al. (2017) Mapping Extracellular pH of Gliomas in Presence of Superparamagnetic Nanoparticles: Towards Imaging the Distribution of Drug-Containing Nanoparticles and Their Curative Effect on the Tumor Microenvironment. Contrast Media Mol Imaging 2017:1–15.
34. Taylor S, et al. (2015) Microenvironment acidity as a major determinant of tumor chemoresistance: Proton pump inhibitors (PPIs) as a novel therapeutic approach. Drug Resist Updat 23:69–78. [PubMed: 26341193]

35. Corbet C, Feron O (2017) Tumour acidosis: from the passenger to the driver's seat. Nat Rev Cancer 17(10):577–593. [PubMed: 28912578]

Statement of significance

GBM tumors exhibit a metabolic gradient that should be taken into consideration when designing therapeutic strategies for treatment. We find differences in metabolomic content in different portions of the GBM tumor, which should be taken into consideration for therapeutic strategies in the treatment of GBM.

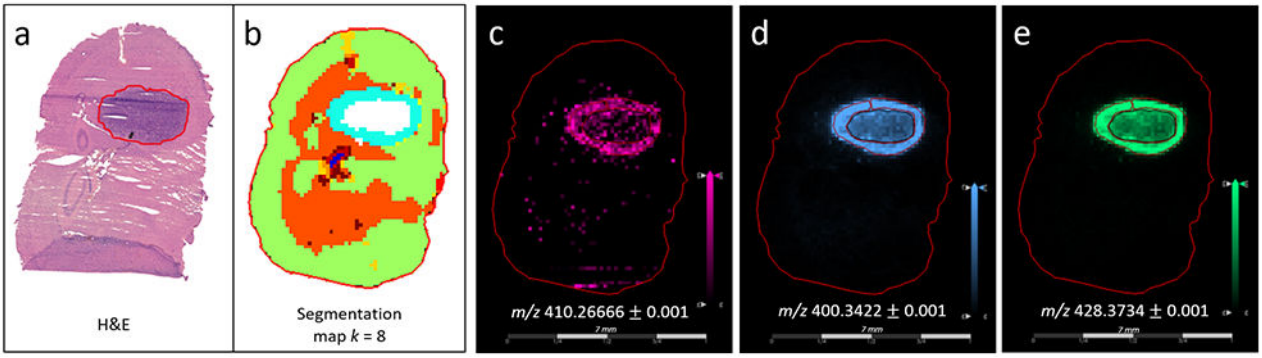

Fig. 1.

MALDI MSI analysis of intracranial GBM12 PDX model: a) H&E stained serial tissue section demonstrating highly cellular tumor region, b) segmentation map of MALDI MSI data produced via bisecting k-means clustering (k = 8), whereby different clusters are labelled with different colors, and two separate clusters are indicated within the tumor region indicating spectral differences between these regions, c-e) MALDI MSI ion images of three different long chain acylcarnitines: c) myristoylcarnitine: *m/z* 410.2666, detected as [M+K] + , d) palmitoylcarnitine: *m/z* 400.3422, detected as [M+H]+ , and e) stearoylcarnitine: *m/z* 428.3734, detected as [M+H]+ .

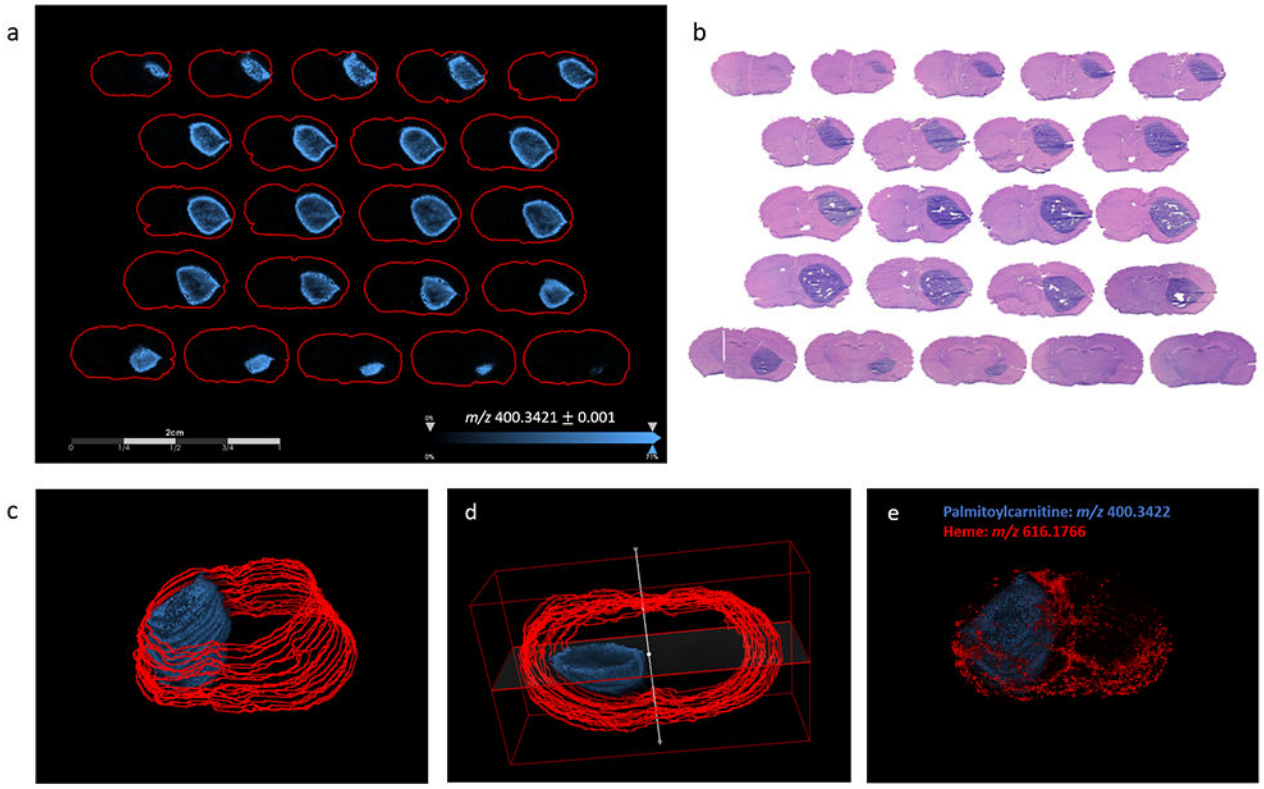

Fig. 2.

3D MALDI MSI of intracranial GBM12 PDX model, a) MALDI MSI ion images of *m/z* 400.3421 corresponding to palmitoylcarnitine in sequential coronal tissue sections taken in increments of 160 μm in the z-dimension throughout the tumor-containing portion of the mouse brain, b) serial tissue sections to those used for MALDI MSI stained with H&E, indicating the highly cellular tumor region, (c & d) 3D reconstructions of images shown in panel (a), shown from different elevations, and e) overlaid with ions of heme (*m/z* 616.1766) demonstrating the distribution of palmitoylcarnitine relative to the vasculature. NB red lines in panel c and d indicate the outer boundary of tissue sections, whereas in panel e red represents heme signature.

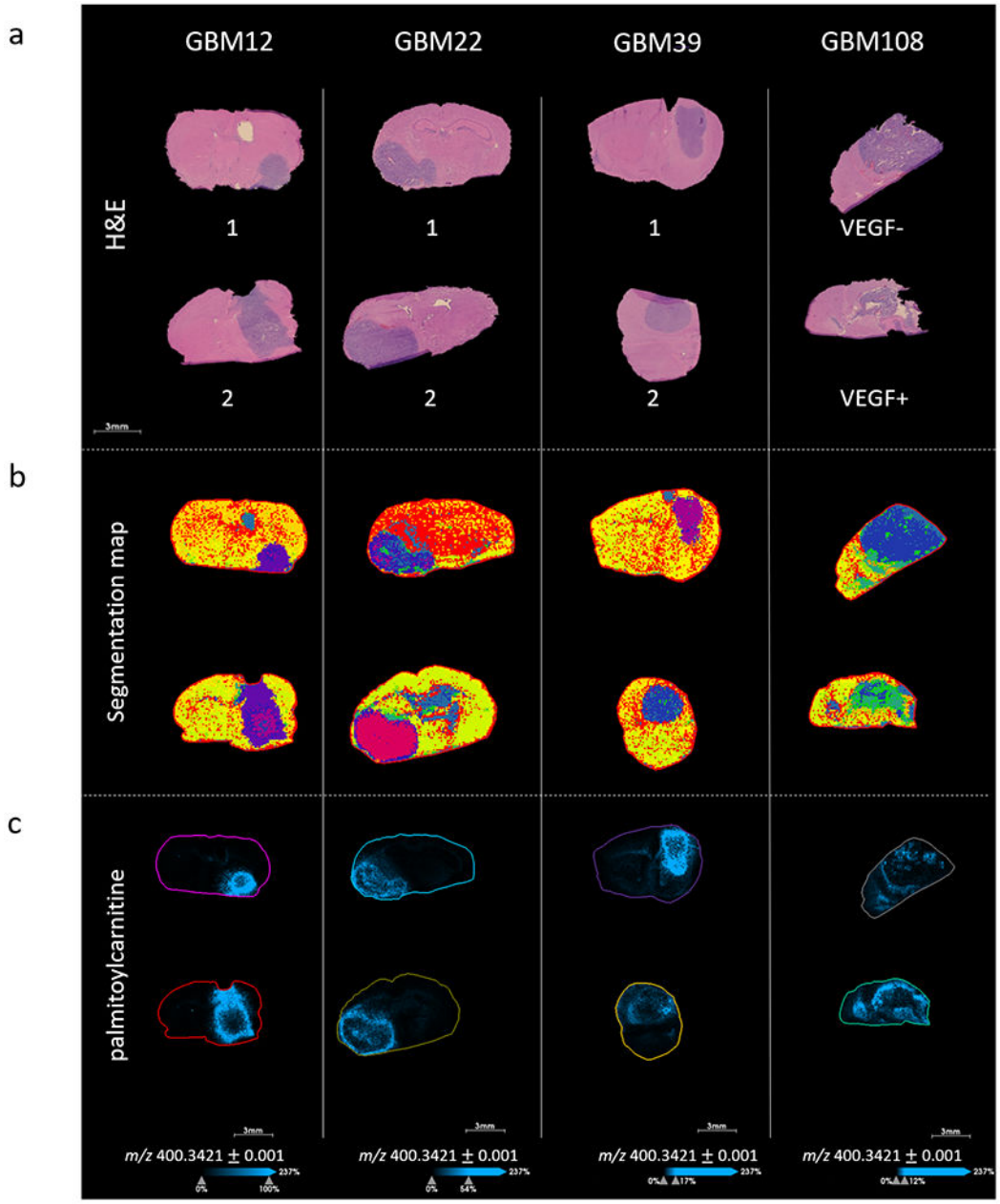

Fig. 3.

MALDI MSI of GBM12, GBM22, GBM39 and GBM108 intracranial PDX models, a) H&E stained serial sections, b) segmentation map of MALDI MSI data, produced via bisecting *k*-means clustering ($k = 8$), c) MALDI MSI ion images of palmitoylcarnitine (m/z 400.3420) in the four GBM PDX models (n=2) showing the relative distribution of long chain acylcarnitines.

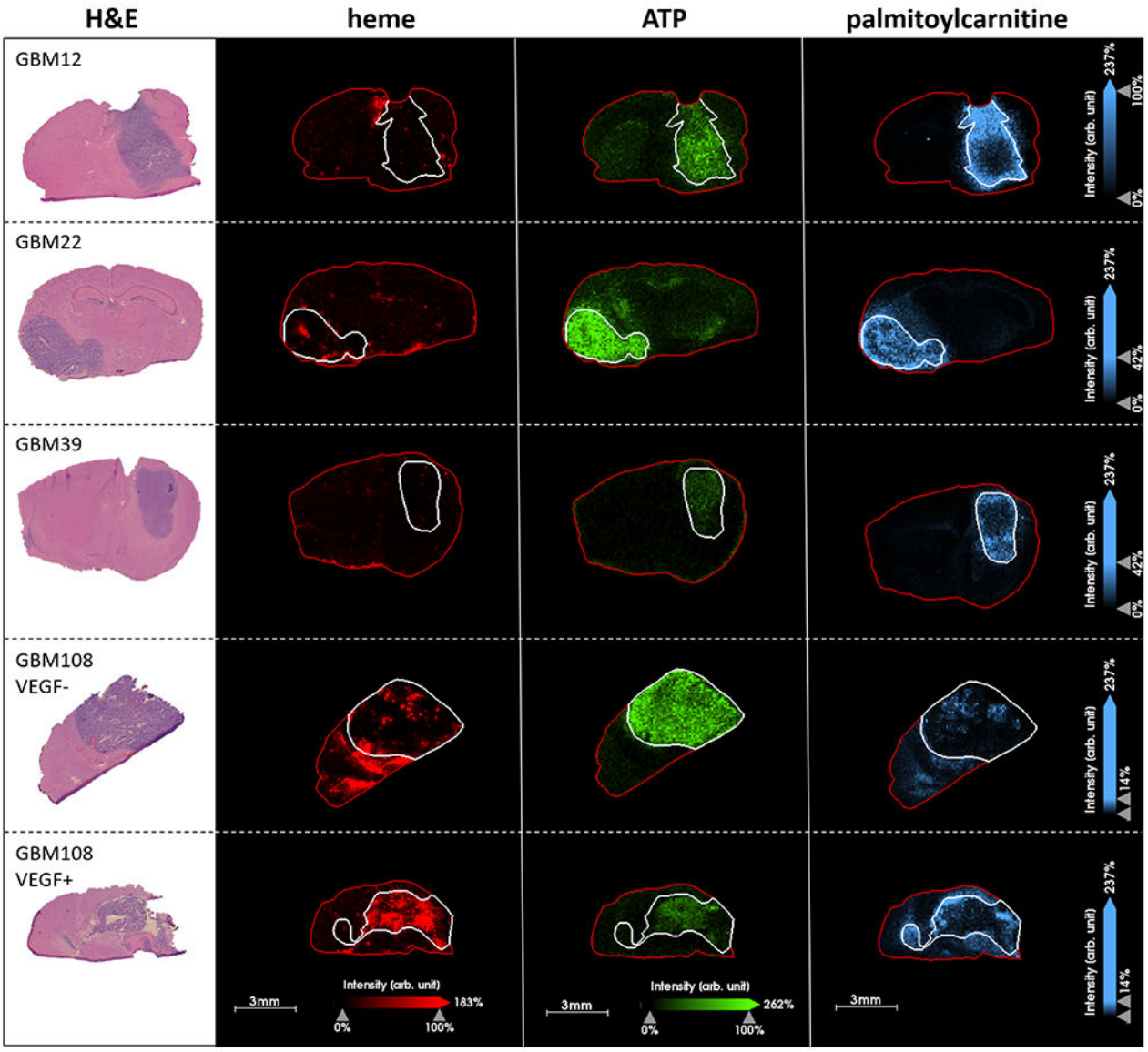

Fig. 4.

MALDI MSI of GBM12, GBM22, GBM39 and GBM108 intracranial PDX models with H&E stained serial sections, comparison of distribution of heme (*m/z* 616.1766, shown in red) indicating the localization of the vasculature, ATP (*m/z* 508.0030, shown in green) and palmitoylcarnitine (*m/z* 400.3420, shown in blue).

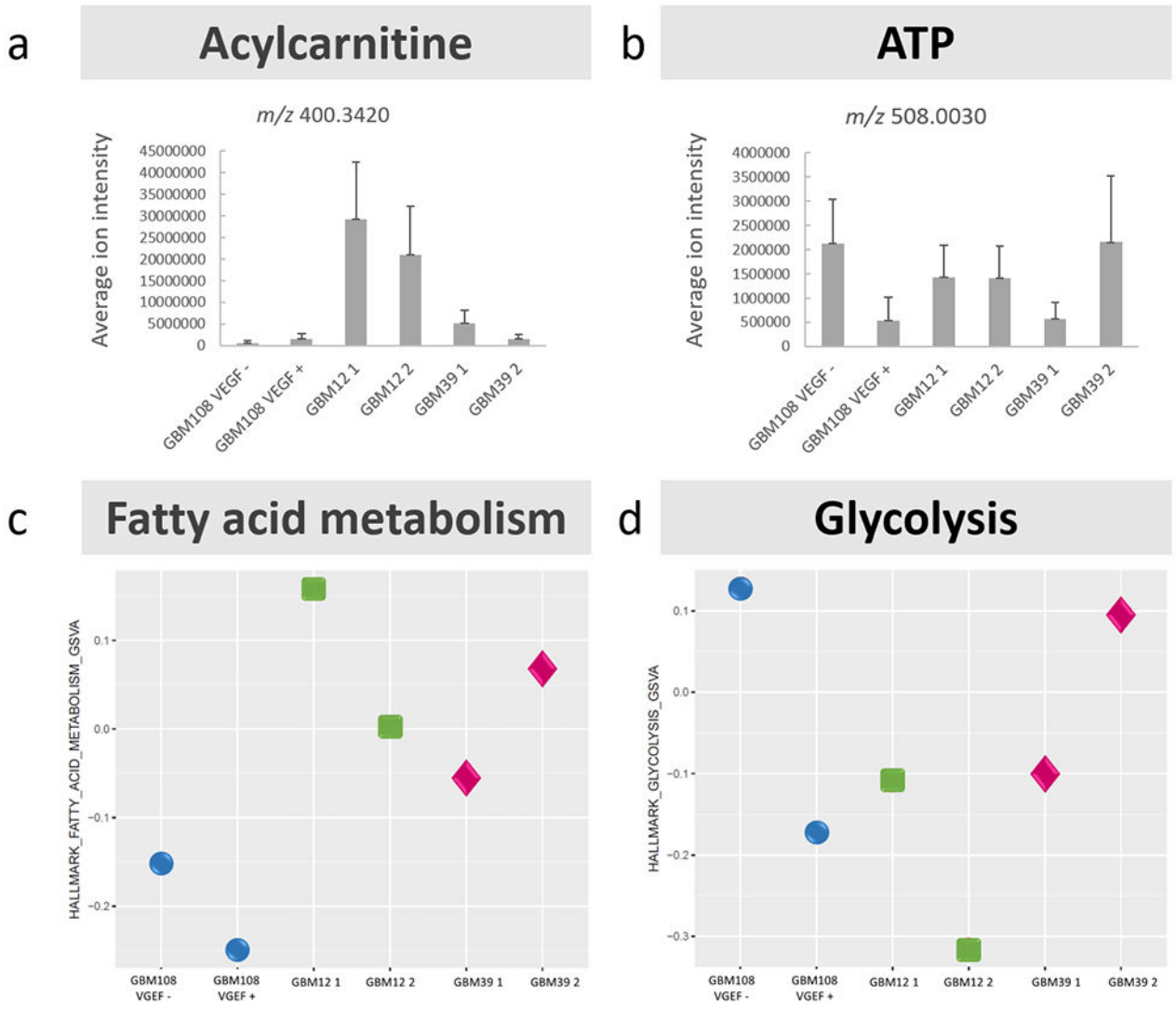

Figure 5.

Comparison of MALDI FT-ICR MSI and transcriptomics data; a-b) Graphs depicting average (mean) ion intensity of m/z 400.3420 and 508.0030 respectively, over the tumor region in each patient-derived xenograft model of glioblastoma, detected by MALDI FT-ICR MSI, error bars represent 1 standard deviation of the mean, c) GSVA plot of HALLMARK genes for fatty acid metabolism in the same set of GBM PDX models, d) GSVA plot of HALLMARK genes for glycolysis. In general, models associated with high levels of acylcarnitine by MALDI MSI have higher expression of hallmark genes for fatty acid metabolism (GBM12) and models/samples with higher levels of ATP measured by MALDI MSI have higher expression of hallmark genes for glycolysis (GBM108 VEGF - and GBM39 2).

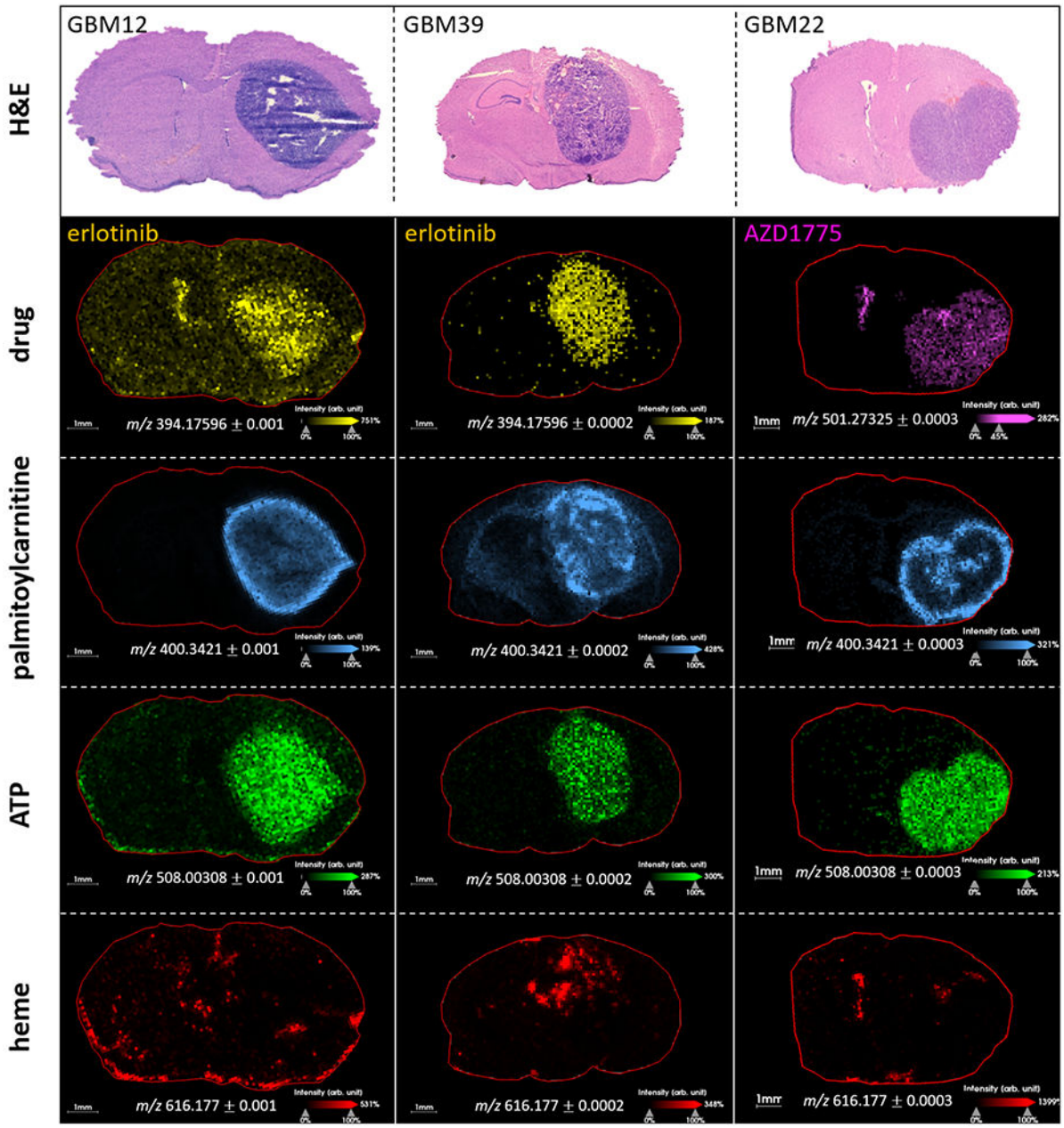

Fig. 6.

Distribution of drugs (erlotinib: *m/z* 394.1770 and AZD1775: *m/z* 501.2733) relative to palmitoylcarnitine (*m/z* 400.3421), ATP (*m/z* 508.0031), heme (*m/z* 616.1766) and H&E images of serial sections. Higher intensity of both drugs was detected in the tumor regions of all PDX models. In GBM12, lower erlotinib intensity is detected at the tumor edge, correlating with regions of high acylcarnitine content. A similar inverse relationship between palmitoylcarnitine and erlotinib was observed in GBM39. AZD1775 was detected relatively homogeneously throughout the tumor, including at the tumor edge, where acylcarnitine intensity was high. ATP was detected with increased intensity in tumor regions of all PDX models, and with an inverse distribution to palmitoylcarnitine.

Table 1.

Summary of acylcarnitines detected from GBM12 PDX models, with associated *m/z* measured, area under the curve (AUC) measured by ROC analysis between tumor core and tumor edge, the p-value measured by t-test for difference in average intensity of the ion between tumor core and tumor edge, the proposed identity of this ion and the Δppm associated with this assignment. Data used to perform the t-test was a random subset of 100 datapoints (pixels) from the tumor edge and the tumor core of the mass spectrometry image presented in Figure 1 (from one GBM12 patient-derived xenograft model).

m/z_{meas}	AUC (ROC analysis)	P-value (t-test)	assignment	Ion or adduct detected	m/z_{calc}	Δppm
400.3422	0.93	<0.001	Palmitoylcarnitine	$[M+H]^+$	400.3421	0.25
428.3730	0.90	<0.001	Stearoylcarnitine	$[M+H]^+$	428.3734	0.93
398.3263	0.86	<0.001	9-Hexadecenoylcarnitine	$[M+H]^+$	398.3265	1.26
410.2667	0.82	<0.001	Myristoylcarnitine	$[M+K]^+$	410.2667	0
448.3419	0.77	<0.001	O-arachidonoylcarnitine	$[M+H]^+$	448.3421	0.40
414.3580	0.71	<0.001	Heptadecanoylcarnitine	$[M+H]^+$	414.3578	0.48
424.3421	0.45	<0.05	Linoelaidyl carnitine or Linoleyl carnitine	$[M+H]^+$	424.3421	0.24